Available online at www.sciencedirect.com
SCIENCE DIRECT®
Journal of Contaminant Hydrology 84 (2006) 36–54
JOURNAL OF Contaminant Hydrology
www.elsevier.com/locate/jconhyd

Quantitative imaging of contaminant distributions in heterogeneous porous media laboratory experiments

J.D. McNeil [a], G.A. Oldenborger [b], R.A. Schincariol [c,*]

[a] *Golder Associates Ltd., London, Ontario, Canada*
[b] *Department of Geosciences, Boise State University, Boise, Idaho, USA*
[c] *Department of Earth Sciences, University of Western Ontario, London, Ontario, Canada N6A 5B7*

Received 10 June 2005; received in revised form 24 November 2005; accepted 10 December 2005

Abstract

Intermediate-scale laboratory experiments on heterogeneous porous media have been increasingly used for the study of saturated and unsaturated ground water systems. While the ability to reproduce field-scale heterogeneity in these experiments has advanced, the use of visualization or image analysis methods to characterize the spatial distribution of solute concentrations has largely remained at the homogeneous media level. To advance these imaging techniques we developed a generic image analysis package that, for the first time, automatically segments regions in photographic images that require unique concentration calibration curves due to varying porous media properties or lighting nonuniformities. As a robust test, our image analysis package was applied to an intermediate-scale flow tank experiment characterized by a correlated random permeability field with unprecedented resolution. Twenty-five distinct classes of porous media were developed and binned to the synthetic permeability field, creating an experimental field of 3456 rectangular cells and thereby ensuring the emplaced field closely matched the statistics of the original continuous distribution. Concentration distributions were determined for an experimental tracer run and the corresponding dispersion parameters were calculated. The closeness of the experimental, image-processed longitudinal dispersivity (4.6×10^{-2} m) to that obtained from the field statistics (9.1×10^{-2} m) verifies our image analysis technique.

Keywords: Ground water; Dispersion; Image analysis; Contaminant plumes; Laboratory studies; Physical models

* Corresponding author. Fax: +1 519 661 3732, +1 519 661 3198.
E-mail address: schincar@uwo.ca (R.A. Schincariol).

0169-7722/$ - see front matter © 2005 Elsevier B.V. All rights reserved.
doi:10.1016/j.jconhyd.2005.12.005

1. Introduction

Laboratory-scale heterogeneous media flow tank experiments have been used extensively in the recent past to study miscible and immiscible contaminant transport processes in saturated (e.g., Silliman and Simpson, 1987; Kueper et al., 1989; Schincariol and Schwartz, 1990; Dullien and Dong, 1996; Swartz and Schwartz, 1998; Chao et al., 2000) and unsaturated (e.g., Wildenschild and Jensen, 1999; Ursino et al., 2001; Oostrom et al., 2003) ground water systems. These experiments have provided invaluable insight enabling the testing of fundamental dispersion theories and numerical models in highly controlled and characterized environments. Furthermore, intermediate-scale two-dimensional (2-D) heterogeneous laboratory experiments have been combined with numerical modeling to test models and address a key underlying calibration and scaling assumption—that heterogeneity explicitly represented, with parameter values applied at the same scale as they are measured, will produce accurate flow and transport predictions (Barth et al., 2001). However, addressing this issue requires controlled heterogeneous experiments with quantitative observations of flow and transport and a complete description of the heterogeneous structure. Simmons et al. (2002) and Silliman et al. (1998) give excellent reviews of the use of porous media laboratory experiments to this end.

Flow and transport observations are routinely made using a variety of tracers (dyes) that allow visual qualitative, and in some cases quantitative, evaluations of plume evolution. Optical tracers such as Rhodamine WT (Schincariol and Schwartz, 1990; Swartz and Schwartz, 1998; Simmons et al., 2002), Fluorescein (Oostrom et al., 1992a,b), or Eosin B (Wildenschild and Jensen, 1999) have been used. Usually the plume is observed in 1- or 2-D experiments along a transparent wall. However, Gheith and Schwartz (1998) and Lee et al. (2003) have extended viewing to 3-D using miniature glass wells and a 7-mm-diameter CCD camera. Quantification of concentration distributions is traditionally done in flow tank studies using small-scale samplers to extract fluid for analysis. Tracers such as potassium bromide, tritium (Barth et al., 2001) or sodium chloride (Swartz and Schwartz, 1998) are used. Alternatively, concentrations can be determined using electrode arrays (Silliman and Simpson, 1987), magnetic resonance imaging (Oswald et al., 1997) or using a high-end, non-intrusive, dual-energy gamma radiation system (Oostrom et al., 2003). However, like all sampling techniques, these methods have potential problems. First is the question as to whether the sampler, electrode, or the process of fluid extraction will influence the contaminant transport. This can be particularly problematic in variable density flow systems where small perturbations to flow can generate instabilities (Schincariol, 1998). A second problem is that discrete point sampling provides only limited sampling spatially, and the time required to collect samples limits sampling temporally. Thus, the usual quantitative observations are via simple breakthrough curves or 1-D cross-sections across plumes.

In order to quantify spatially complex, variable density plume instabilities, Schincariol and Schwartz (1990) employed low-level image analysis techniques and were able to distinguish a 10% to 25% and a 50% to 100% source concentration zone in their photographic images. The image analysis techniques were later significantly advanced, for homogeneous porous media, by Schincariol et al. (1993) to allow for a much finer segmentation of the concentration distribution. These imaging techniques were later employed by Swartz and Schwartz (1998). While Schincariol et al. (1993) developed a framework to correct for differences in grain diameter and pore size, and thus dye concentration in heterogeneous media experiments, they were not tested due to a lack of calibration images from Schincariol and Schwartz (1990).

Furthermore, this framework, being entirely manual, could only be realistically applied to very simple heterogeneous fields (e.g., layered systems) that possessed little or no variation in material properties or lighting within a designated porous medium class. Ursino et al. (2001) corrected the images for spatially inhomogeneous light conditions but no correction was employed to account for the effects of different grain diameters and pore sizes on dye concentration.

One of the key problems with correcting for varying media properties during image analysis is the need for separate calibration curves for each type of porous medium and precise control of lighting nonuniformity. Thus, the objective of this research was to develop a simple generic image analysis algorithm that could automatically detect those regions in photographic images that require separate calibration curves due to varying porous media properties (e.g., grain size, grain distribution and color) or lighting nonuniformities. Thus the number of calibration curves is determined solely by the characteristics of the permeability field and tank/lighting conditions. If necessary, calibration curves can vary in time as field properties change (e.g., via precipitation or staining). As a robust test, our image analysis algorithm was applied to an intermediate-scale flow tank experiment characterized by a correlated random permeability field of sufficient correlation lengths to meet ergodic requirements (Welty and Elsner, 1997). While previous heterogeneous flow tank experiments have used two (Oostrom et al., 2003), three (Ursino et al., 2001), or five (Barth et al., 2001), different porous media size fractions to represent the permeability distribution, we have employed 25 distinct classes of porous media. This resolution enables the correlation structure of the discretized distribution to closely match the corresponding statistics of the original continuous distribution, thereby facilitating numerical and statistical model comparisons.

It should be noted that while our techniques are presented for reflected light images, they should be easily adaptable to transmitted light experiments involving non-uniform media properties. Transmitted light techniques (Tidwell and Glass, 1994; Detwiler et al., 1999) require very thin slab systems and even with advanced transmitted light image analysis (Darnault et al., 2001) the technique still requires uniform homogeneous sand packing for accurate calibration.

2. Intermediate-scale flow experiment

The first part of this section provides a brief summary of the flow tank construction and a description of the generation, discretization and emplacement of the heterogeneous porous media. The image acquisition techniques and image analysis theory and processing algorithms are discussed in the second and third parts of this section, respectively.

2.1. Experimental tank

The flow tank was constructed of transparent 19.05 mm thick Polycast® acrylic sheets and is modular in design to allow variable flow lengths (Fig. 1). In order to meet the targeted ergodic constraints, all five modules were used throughout the experiments described herein. Stainless-steel tension pins prevent significant deformation of the acrylic walls allowing minimal exterior structural reinforcements and maximum viewable area. The flow tank consists of three distinct sections: an influent chamber, a flow chamber (internal dimensions 6.25 m length × 1.25 m height × 0.05 m depth) and an effluent chamber. The influent chamber is divided up into ten reservoirs, each connected to separate channels of a high precision peristaltic pump (Ismatec®

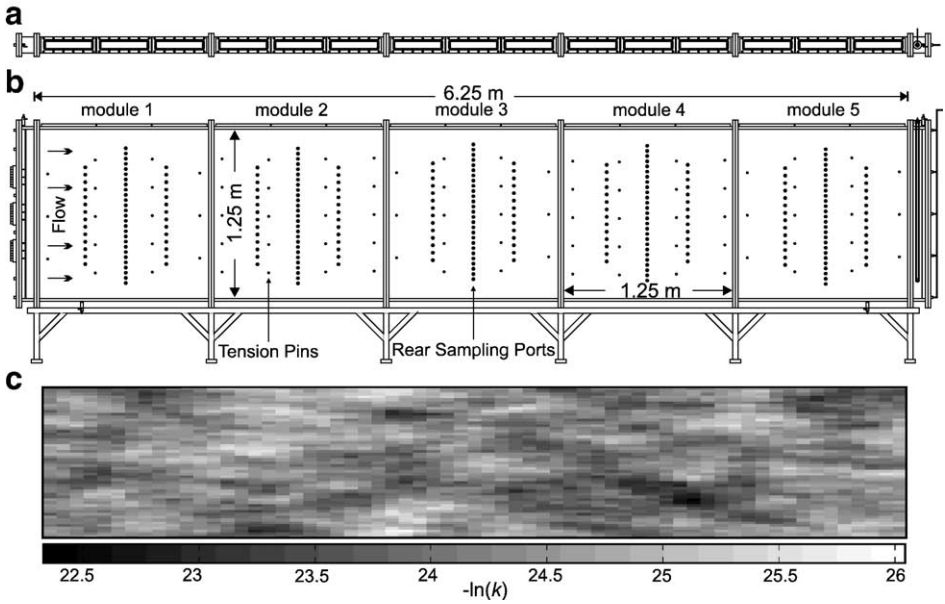

Fig. 1. Assembled acrylic modular flow tank. a) Top view. b) Front view. c) Correlated synthetic permeability field. Dark regions are more permeable.

Sa IPC) connected under positive pressure to de-aired/de-ionized water or tracer, allowing balanced flow rates to be delivered to each reservoir. Porous stainless-steel plates (1.6 mm thick, 50% interconnected porosity, 20 μm pore diameter) prevent the porous media from entering the influent and effluent chambers. Experiments were run under saturated conditions with a constant-head discharge point located above the effluent chamber.

A synthetic heterogeneous permeability field was generated using the spectral techniques developed by Robin et al. (1993). The permeability (k) distribution follows a log-normal probability density function and is characterized by a mean $\{\ln(k)\} = -24.3$ (m^2) and variance $\sigma^2_{\ln(k)} = 0.24$. The field exhibits a weakly-stationary, spatially-correlated structure defined by an exponential covariance function with horizontal and vertical correlation scales of $\tau_x = 0.38$ m and $\tau_z = 0.06$ m, respectively. These correlation scales were chosen to be representative of typical intermediate-scale field values (Sudicky, 1986) and to satisfy the ergodic requirement within the length constraints of the tank (Welty and Elsner, 1997). A permeability cell size of 0.096 m in the horizontal direction and 0.02 m in the vertical direction results in 4 cells per correlation length, horizontally, and 3 cells per correlation length, vertically. Cell dimensions were chosen both considering a practical limitation for the size of individual porous media cells to be emplaced in the tank and to ensure sufficient reproduction of the covariance structure (Ababou et al., 1989; Welty and Elsner, 1997). The generated synthetic 64×54 cell permeability field is shown on Fig. 1(c).

In order to reproduce the synthetic permeability field in the tank, custom blends (classes) of glass beads (Flex-O-Lite Inc.) with grain diameters ranging from 0.06 to 0.6 mm were developed. The permeability of each bead class was determined by taking the average of nine individual constant head permeameter tests (three random samples each tested at three different head values). Through a trial-and-error approach, 25 unique classes of porous media were

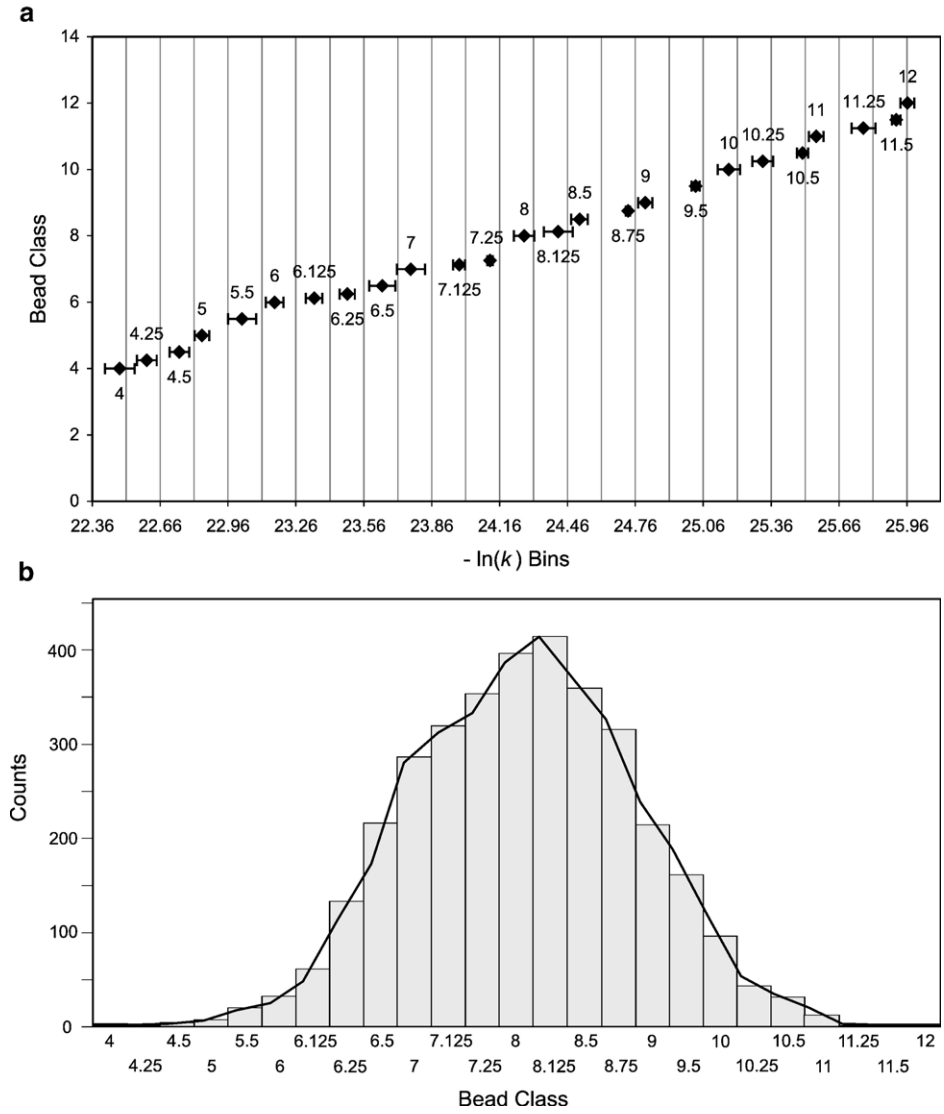

Fig. 2. Permeability (k) and bead class information for the 25 porous media classes emplaced in the flow tank. (a) Permeability range of porous media classes where the bead class designation represents a mixing formulation based on standard size fractions available from the manufacturer. Horizontal bars represent the measurement error for k. (b) The frequency distribution of the 25 porous media classes categorized using a mixing class descriptor and overlain by the distribution curve for the ln(k) values of the synthetically generated permeability field.

developed and binned to the synthetic field (Fig. 2a). A bin width of 0.15, with values of $-\ln(k)$ ranging from 22.36 to 26.22 (m^2), provided adequate separation of the measured permeability values. This method of correlation provided an extremely accurate reproduction of the synthetically generated field (Fig. 2b). A template grid of 64 columns and 54 rows, corresponding to 3456 rectangular cells of dimension 0.096×0.020 m, and specialized emplacement dividers were used to accurately emplace the porous media under a constant head of water (Fig. 3). A low permeability layer (thin layer of the lowest k porous medium)

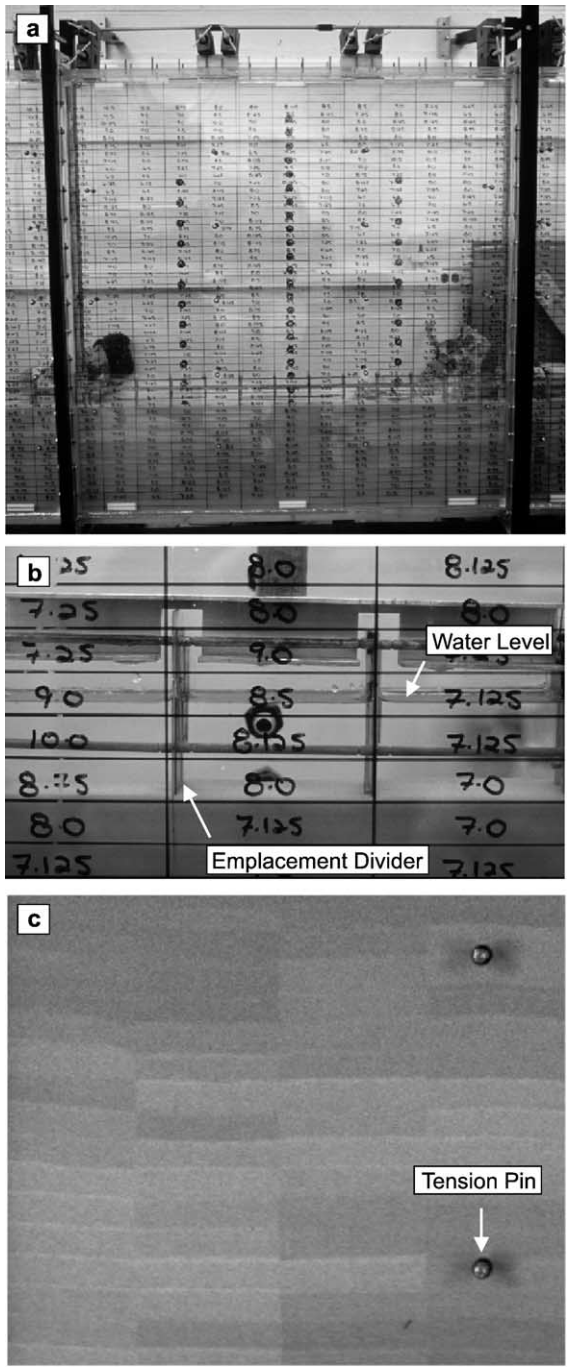

Fig. 3. Porous media cells. (a) Image showing the emplacement dividers and emplacement process. (b) Close up of single divider; the distance between dividers is 9.6 cm. (c) Image showing a portion of the emplaced permeability field; each cell is 9.6 × 2 cm.

followed by a layer of bentonite and an inflatable water bladder, prevented any short-circuiting of flow across the top of the tank. A thin low permeability layer was also placed along the bottom of the tank. Details of emplacement/experimental techniques can be found in McNeil (2004).

2.2. Image acquisition

Although the image analysis procedure discussed below corrects for small variations in lighting across an image, uniform lighting will improve the quality of any optical observations. Since concentration calibration images must apply to all subsequent flow tank experiments, consistency in lighting is required. To this end, four Lowel® Tota-light 500 W 3200 K tungsten halogen lights with reflection umbrellas were positioned to provide even lighting on a tank module. Lighting adjustments were made until the vertical and horizontal lighting variations were within a target value of 1/3 of an *f*-stop, the camera meter sensitivity limit, when measured on an 18% gray card.

Image positives (Kodak® Ektachrome 64T) were scanned using a Nikon® Super Coolscan 4000 ED at a spatial resolution of 3000 pixels per inch and a color resolution of 14 bits per channel, yielding a total bit range of 16,284 possible intensities (brightness values). Maximum bit range is required to show detail in the dark regions of the image without the bright areas becoming saturated. Images were then separated into individual color channels (red, green and blue) and the green spectrum was extracted as the image variable. Scalar (monochromatic) images are required for analysis and the green spectrum was selected due to its high sensitivity to Rhodamine WT concentration, as evidenced by the maximum contrast in intensity values between the background porous media and the tracer (Fig. 4).

2.3. Image analysis

In the current context, image analysis refers to the use of variations in brightness, or intensity, within a digital image as a means of identifying features of interest. The fundamental assumption is that similar features will have similar brightness. A particular brightness value is thus representative of a particular feature and can be used to make qualitative and quantitative observations. The theory and operational considerations behind this image analysis strategy, often referred to as brightness thresholding, are discussed in general by Russ (1999) and in regards to flow tank experiments by Schincariol et al. (1993).

The image analysis software was developed as a flow visualization tool to permit the optical determination of tracer concentration in flow tank experiments with generally heterogeneous media. The processing steps (Fig. 5) were implemented in the MATLAB® environment to allow for portability and ease of customization; the script package can be obtained by contacting the authors. The basic image analysis protocol includes the following steps which will be elaborated on: (1) digitization of film images or direct digital capture; (2) rotation and transformation of images to standard dimensions; (3) standardization of image intensity to optical density; (4) optional median filter; (5) background leveling; (6) median filter; (7) calibration of optical density to dye concentration; and (8) conversion of optical density images to concentration distributions. However, to accommodate generally heterogeneous media, an image segmentation step must be incorporated into the basic image analysis protocol described above. This additional step represents a significant advancement and allows the work of Schincariol et al. (1993) to be extended to generalized heterogeneous media.

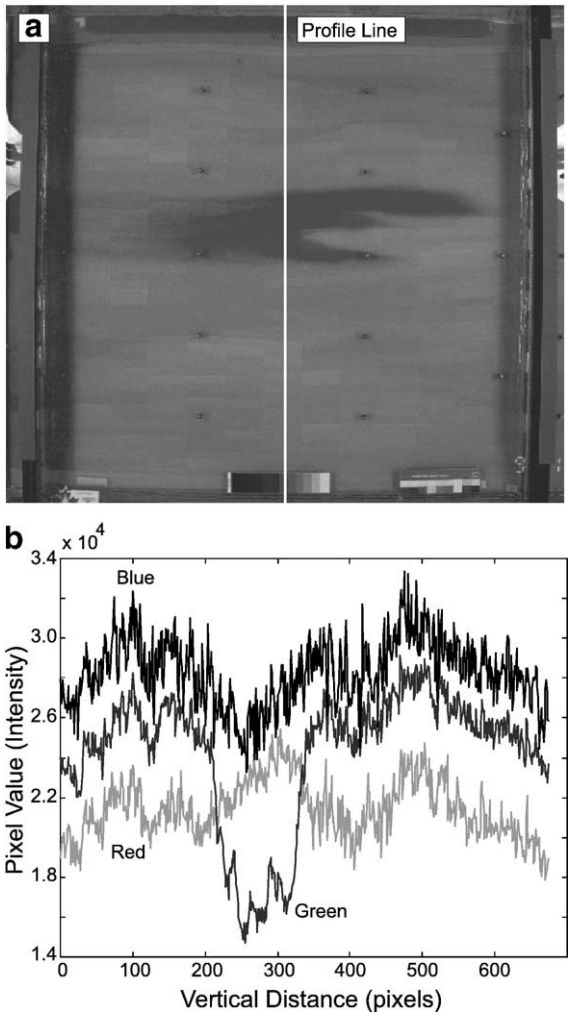

Fig. 4. Analysis of the spectral contrast between the tracer pulse and the background porous media in module 1 after 20 h of transport. The location of the profile is shown in (a). (b) The signal is split into the individual color channels (blue, green, red) and the pixel value (intensity) is plotted as a function of vertical distance (pixels).

In the first stages of image analysis, images must be standardized to optical density because variations in lighting, exposure and film development result in non-uniform image intensity between successive images. Photographic theory is largely developed in terms of transmittance, a ratio of the intensity of transmitted to incident light. A necessary assumption is that image intensity (in this case the magnitude of the green spectrum) is directly proportional to transmittance. In this case, optical density D is related to intensity I by:

$$D = \log_{10}(a/I) \tag{1}$$

where a is simply a constant of proportionality. Thus, a calibrated grayscale present in each image provides known optical density values that are used to develop an I–D calibration curve for each image. We use non-linear, least-squares optimization to determine either the parameter

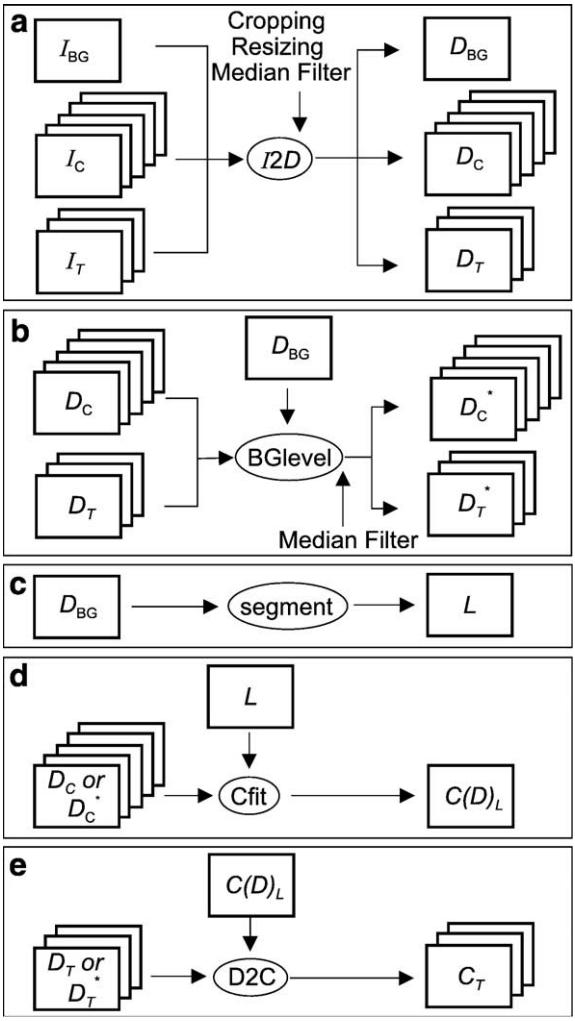

Fig. 5. Flow chart for the image analysis suite of algorithms. The input images are a background image I_{BG}, a deck of constant concentration calibration images I_C, and a deck of tracer (time series) images I_T. The processing flow moves from top to bottom and the output (on the right side) of each step is used as input (on the left side) to the subsequent step. (a) Conversion of intensity to optical density. (b) Optional background leveling. (c) Segmentation of background optical density into optically distinct interval L. (d) Construction of leveled or non-leveled functional D–C calibration curves for each interval of L. (e) Conversion of optical density to tracer concentration.

a of Eq. (1) or the coefficients of a generalized power law (Fig. 6). Generally, the power law provides a more precise fit because it is able to accommodate errors associated with the assumption that intensity is directly proportional to transmittance; power law calibrations are utilized hereafter.

After standardization to optical density, it must be decided whether or not to apply a median filter (Schincariol et al., 1993) or background leveling. Optical densities are additive and, therefore, leveling has the potential to isolate the tracer plume by subtraction of a background image with no tracer from an image with tracer present. Background leveling is often needed to correct images which may have brightness variations due to non-uniform lighting, non-planar

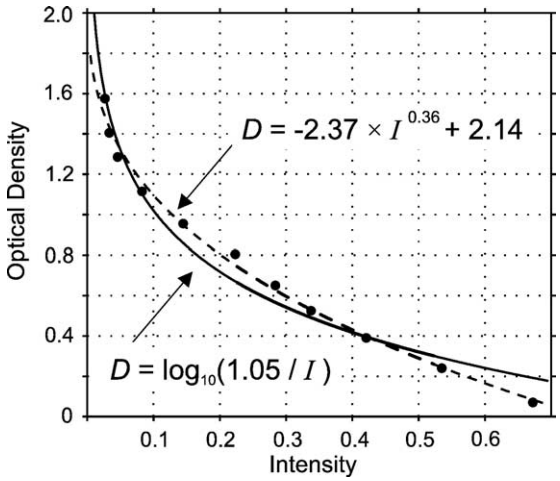

Fig. 6. Least-squares calibration of optical density to image intensity (normalized green spectrum) using the theoretical log function (solid line) and a general power law function (dashed line). The calibration is for the background image of module 1 (Fig. 7a).

surfaces, or variations in camera/digitizer response. Further, background leveling will also correct for the observed color variation between the porous media classes. However, leveling can reduce dynamic range, effectively discarding some of the original data and invariably adds noise (Russ, 1999).

Even with background leveling, the different porous media classes result in varying fluid thicknesses adjacent to the tank wall, and the optical density value of a dye is proportional not only to the tracer concentration, but also to its thickness. For these reasons, multiple optical density–concentration (D–C) calibration functions are required (possibly one for each porous medium class) in order to determine the concentration distribution of a tracer in an image. This becomes a prohibitive step in an image analysis algorithm if we imagine keeping track of porous media class locations, especially when the porous media are observed to deform and shift somewhat after emplacement (Fig. 3c). To accommodate generally heterogeneous media, an image segmentation algorithm was developed that segments a background optical density image into a number of optically distinct regions each belonging to a particular interval of the range of D. The rationale is that each optically distinct region will require a unique D–C calibration and that if different materials are not optically distinct, they will not require unique D–C calibrations.

We note that each porous medium class may not necessarily occupy a separate D interval. Some classes of media will fall in the same D interval while separate D intervals may contain portions of the same medium class due to lighting nonuniformities. Thus, segmenting a background D image would reduce the need for perfect uniform lighting to one of consistent lighting if we were to allow for unlimited optically distinct intervals. However, we choose to limit the number of intervals either by defining a target number of optical density intervals (such as the number of classes of media) or by specifying some a priori estimate of optical density tolerance. Here, we utilize the tolerance concept and employ approximately one-quarter of the increment on our photographic grayscale as the tolerance; the choice of appropriate tolerance is typically arrived at through experience and trial-and-error. The range of optical density in a background image is then segmented into a set of equal intervals (where the interval width is equal to the

tolerance) and each pixel is then designated as belonging to a particular interval. For images containing noise or extraneous information, some D intervals may be populated entirely by noise. Typically, these intervals lie at the extremes of the range of D; an example is the black tension pins that are present in the interior of the spatial domain (Fig. 3c) but are at the extreme limit of the

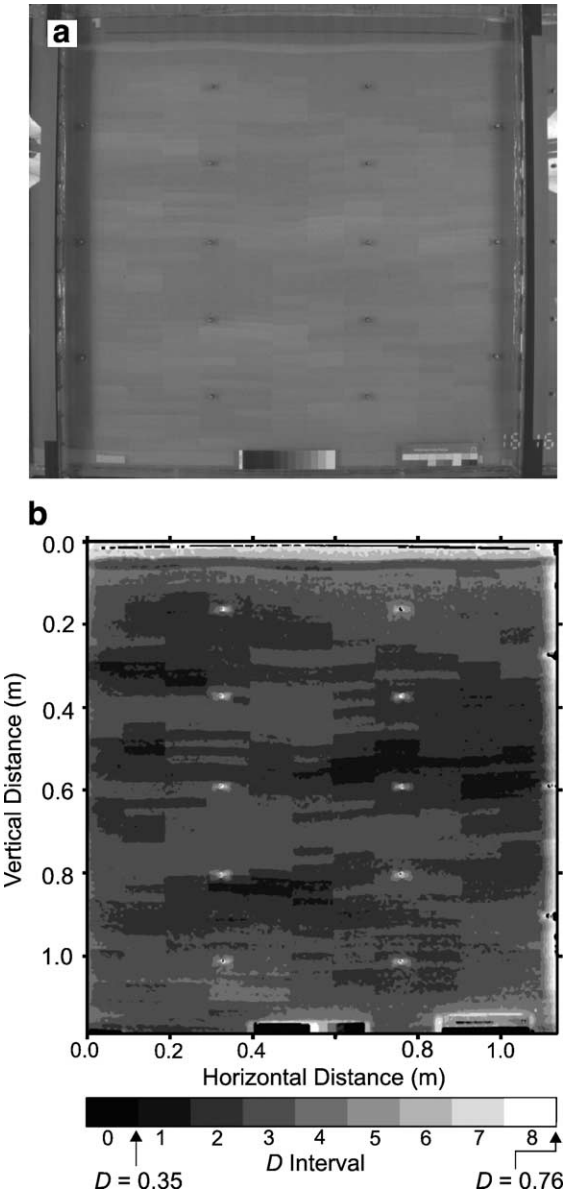

Fig. 7. Segmentation of background optical density into optically distinct intervals. (a) Raw background image of module 1. (b) Segmented optically distinct regions for the background image of module 1. Desegmented pixels are depicted as black but include pixels with values at both the high ($D > 0.76$) and low ($D < 0.35$) limits. Desegmented pixels are limited to tank infrastructure.

range in D. The algorithm is programmed to identify pixels belonging to D intervals that are populated by less than some threshold number of pixels. These noise pixels are then effectively "desegmented" by removing them from the processing flow. The risk of desegmenting a porous medium pixel is very low since the populations of D intervals occupied by media pixels are orders of magnitude greater than those for intervals populated by noise. Regardless, a visual check ensures that desegmented pixels are properly identified. For example, segmenting the background image of module 1 (Fig. 7a) with a tolerance of 0.05 results in 34 optically distinct intervals (Fig. 7b). Desegmentation removes 1.4% of the total number of pixels from the processing flow and 8 optically distinct levels remain. The porous media occupy only a small range in D and this is a major reason for maintaining maximum dynamic range in our images.

Given a segmented image structure, D–C calibration curves can be constructed for each optically distinct interval using the average optical densities (either leveled or non-leveled) and reference concentrations for all pixels in each interval. For the experiment discussed here, continuous full frontal tracer plumes with concentrations of 0, 5, 10, 20 and 40 mg/L Rhodamine

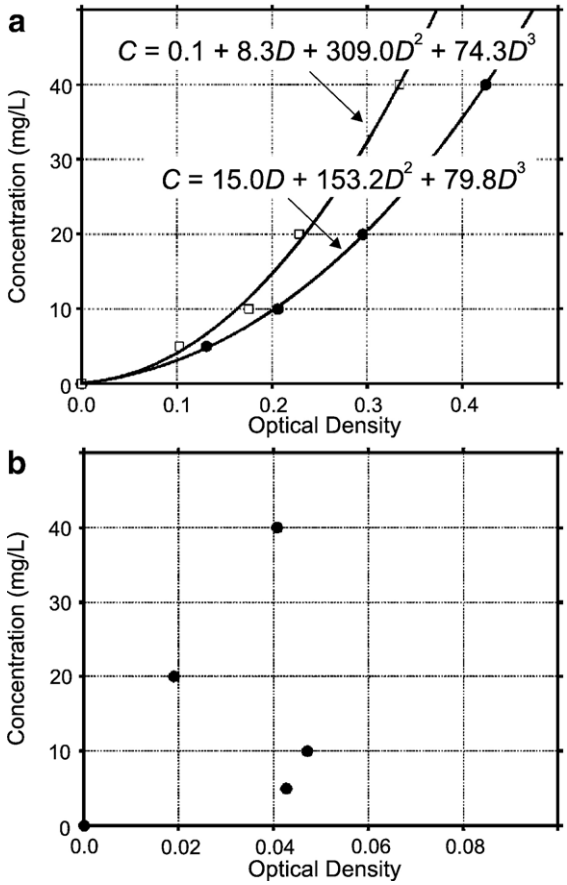

Fig. 8. (a) Leveled optical density–concentration calibration curves for module 1. The calibrations are shown for the first (circles) and fifth (squares) optically distinct intervals of the background image for module 1 (Fig. 7). Note the change in the range of D between the intervals. (b) Leveled optical density–concentration values for desegmented pixels at the lower limit of D.

WT were used. The standard concentration flushes must be continued until the entire field is at the source concentration. For our field, at a flow rate of approximately 5×10^{-7} m^3 s^{-1}, each standard concentration injection required approximately 150 h. Example leveled calibrations are presented as Fig. 8 for the first and fifth optically distinct levels of module 1; clearly, a single calibration curve would be inadequate (e.g., an optical density of 3 translates to 20 mg/L for class 1 but 30 mg/L for class 5). A non-segmented bulk calibration curve was also calculated, and while not shown in Fig. 8, falls just below and nearly mirrors the class 1 calibration curve. Photographic theory (Beer's Law) predicts a linear relationship between optical density and tracer concentration (Williamson and Cumming, 1983); however, as previously discussed, a polynomial or power law often results in a more precise fit. Desegmented pixels exhibit essentially constant optical densities regardless of reference concentration (Fig. 8b). For these pixels, optical density does not vary with changes in concentration; this observation is consistent with desegmented pixels containing extraneous information (e.g., tank infrastructure). The image processing software allows the user to view and verify each of the *D–C* calibration curves and adjust the curve fitting algorithm. With the set of calibration curves for all optically distinct regions, tracer concentration is predicted from optical density over the entire image with a spatial resolution equal to the pixel dimensions (in this case, approximately 0.5×0.5 mm). At this final stage, any desegmented pixels can be returned to the concentration image using a minimum-neighborhood median filter.

3. Application to tank experiment

The image analysis protocol described above was applied to determine concentration maps for an intermediate-scale flow experiment with unprecedented porous media heterogeneity. A flow velocity of 1.24×10^{-5} m s^{-1} was established for the field. After disconnecting a central reservoir of the influent chamber from the water supply, the reservoir was flushed with 40 mg/L Rhodamine WT. Rhodamine WT dye is generally considered a conservative tracer and has been widely used in surface water and ground water studies (Smart and Laidlaw, 1997; Wilson et al., 1986); however, the extent of sorption varies as a function of the dye isomer, aqueous concentration, solution pH, ionic strength and composition, and porous media composition (Kasnavia et al., 1999; Sutton et al., 2001; Vasudevan et al., 2001). With the dye at full concentration, the injection reservoir was connected to a tracer supply using a separate channel of the peristaltic pump, with flux rates equal to the de-aired/de-ionized water flux flowing through the remaining cross-section of the influent chamber. The injection was continued until a tracer pulse was developed with approximate dimensions of 300 mm in the flow direction and 150 mm in the transverse direction. At this point, the tracer injection chamber was again flushed with de-aired/de-ionized water to complete the pulse. However, a small amount of tracer remained in the injection chamber which resulted in a non-perfect pulse truncation and some trailing. The image of this plume in module 1 after 20 h is shown in Fig. 4a. The concentration distribution at 20 h, obtained by employing the image processing routines discussed above, is shown in Fig. 9. Clearly the heterogeneity of the permeability field is already influencing transport and the image analysis routines have accounted for background variability of the porous media. The anomalous dye concentrations visible along the top of the module are remnant tracer from the calibration runs that had not been entirely flushed due to the very low permeability of the top layer. Also, portions of the standard gray card and color patch card are visible at the bottom of the tank and the tension pins have not been entirely eliminated by leveling and desegmentation.

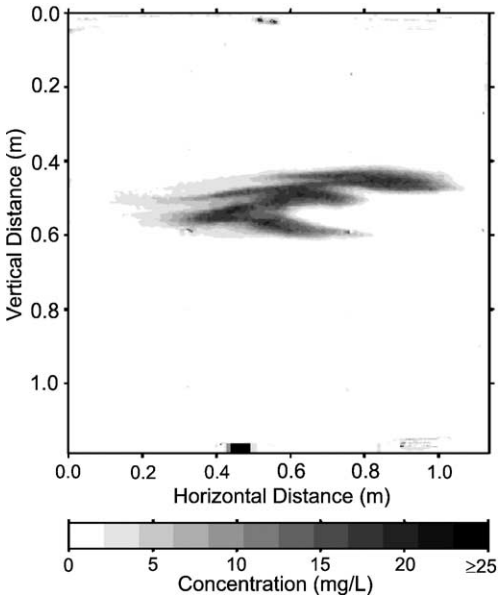

Fig. 9. Plume concentration in module 1 after 20 h (raw image shown on Fig. 4a). The tracer pulse was injected with dimensions of 300 mm in the horizontal direction and 150 mm in the vertical direction. Maximum plume concentration is 25.1 mg/L.

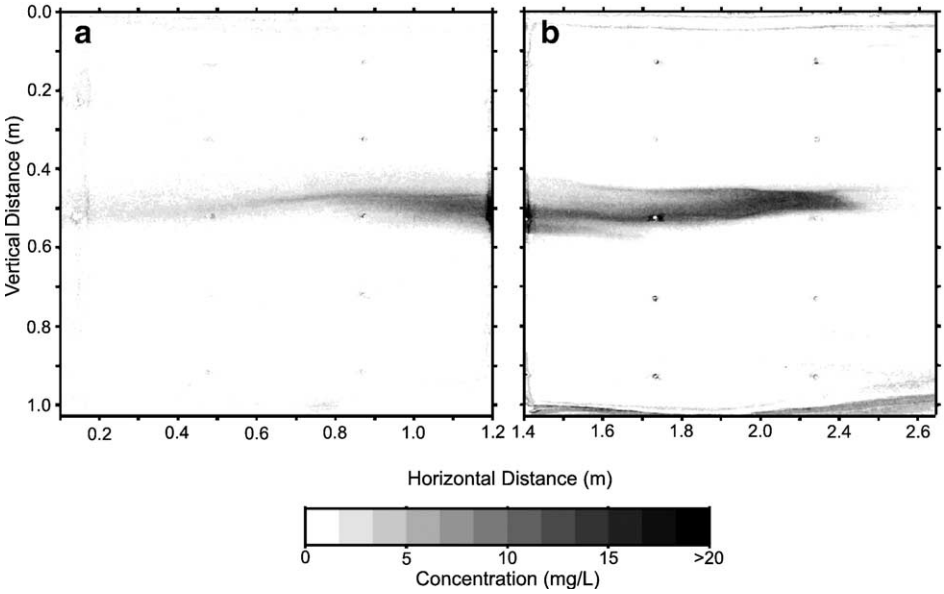

Fig. 10. Plume concentration in modules 3 (a) and 4 (b) after 76 h. The 0.20 m gap between images is due to shadow zones cast by the flanges at the module joints. The effect of these shadow zones on the imaged concentration can be seen at 1.2 and 1.4 m in the horizontal direction.

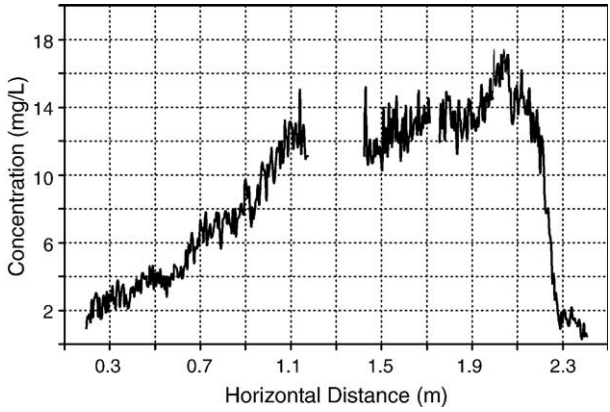

Fig. 11. Concentration as a function of horizontal distance along the plume axis at 76 h within modules 3 and 4 at approximately 0.5 m in the vertical direction. Gaps in the record are due to shadow zones at the flange joint (1.2 to 1.4 m) and a tension pin (~1.75 m).

After 76 h the plume had traveled to and spread over flow tank modules 3 and 4 and had undergone considerable dispersion and elongation due to heterogeneity of the porous medium; the concentration distribution is shown on Fig. 10. The extensive plume present at the bottom of Fig. 10b is a remnant of the full field flush concentration calibration runs traveling in the low permeability bottom layer of the tank. Again, the tension pins are visible both as non-zero concentration (due to incomplete leveling and desegmentation) and as zero concentration (the result of desegmentation). Other tank infrastructure that is not completely removed via subtraction or desegmentation also appears as non-zero concentration and subjective identification of this noise is required. Generally, the largest errors are associated with incomplete or poorly-aligned background leveling.

To further test the image analysis routines, imaged values of Rhodamine WT concentration were plotted in 1-D, at the pixel scale, along the longitudinal axis of the 76 h plume (Fig. 11), and transverse to the plume (Fig. 12). The scatter, or apparent noise, in the concentration signals is partly due to the very fine pixel resolution. Since pixel resolution is on the order of the grain size of the porous medium, some pixels will represent grains, while others will represent pore

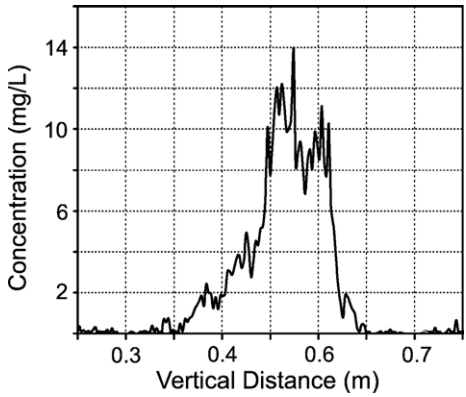

Fig. 12. Concentration as a function of vertical distance perpendicular to the plume axis at 76 h within module 4 at 1.45 m in the horizontal direction.

space. Using these 1-D transects of concentration, the coefficients of longitudinal (D_L) and transverse (D_T) hydrodynamic dispersion can be calculated via the standard relationships (Schwartz and Zhang, 2003; Robbins, 1983):

$$D_L = \frac{\sigma_L^2}{2t} \qquad D_T = \frac{\sigma_T^2}{2t} \tag{2}$$

where σ_L and σ_T are the longitudinal and transverse standard deviations of the concentration distribution at time t. The standard deviations can be determined by the graphical half-maximum method (e.g., Domenico and Schwartz, 1998) or by least-squares fitting of normal curves. Hydrodynamic dispersion values obtained using the graphical method are presented in Table 1; results from normal curve fitting are very similar. The coefficients of hydrodynamic dispersion can be then separated into their component parts of mechanical dispersion and diffusion:

$$D_L = \alpha_L v + D^* \qquad D_T = \alpha_T v + D^* \tag{3}$$

where v is the ground water velocity in direction of flow, α_L and α_T are the longitudinal and transverse dispersivities, and D^* is the bulk diffusion coefficient. Using a bulk diffusion coefficient of 5.6×10^{-10} m^2 s^{-1} (Schincariol et al., 1994) and the measured average ground water velocity of 1.24×10^{-5} m s^{-1}, the dispersivities are calculated and presented in Table 1. It is interesting to note that our α_L value of 4.6×10^{-2} m compares well to the α_L of 1.2×10^{-3} to 6.7×10^{-4} m obtained by Oostrom et al. (1992b) who utilized a gamma radiation system to determine concentrations in flow tank experiments. The smaller α_L values of Oostrom et al. (1992b) are expected as they used uniform sand versus our heterogeneous permeability field. Because the geostatistics of the emplaced permeability field are known, the expected asymptotic longitudinal dispersivity (A_L) can be estimated using the following equation provided by Gelhar and Axness (1983):

$$A_L = \frac{\sigma_Y^2 \lambda}{\gamma^2} \tag{4}$$

where A_L is the longitudinal asymptotic dispersivity, σ_Y^2 is the variance of the log-transformed hydraulic conductivity field, λ is the correlation length in the mean direction of flow, and γ is a flow factor equal to unity (Dagan, 1982). While A_L characterizes the longitudinal dispersivity in the horizontal direction due to the heterogeneous nature of the field, and does not include local pore-scale dispersion components, it should be the major component of the experimental longitudinal dispersivity value obtained from the imaged concentration distribution (Fig. 10). Applying Eq. (4) to the emplaced permeability field results in a value of $A_L = 9.1 \times 10^{-2}$ m for the longitudinal asymptotic dispersivity which is comparable to the experimentally measured longitudinal dispersivity of $\alpha_L = 4.6 \times 10^{-2}$ m. Since the plume has only traveled through approximately 10 correlation lengths, one would expect the experimental longitudinal dispersivity to be slightly smaller than the asymptotic dispersivity. Longitudinal dispersivities reached asymptotic conditions after the plume traveled 10 correlation lengths at Cape Cod (Garabedian et al.,

Table 1
Experimental dispersion results

Parameter	Current investigation
Longitudinal dispersion coefficient, D_L	5.6×10^{-7} m^2/s
Transverse dispersion coefficient, D_T	2.4×10^{-9} m^2/s
Longitudinal dispersivity, α_L	4.6×10^{-2} m
Transverse dispersivity, α_T	1.9×10^{-4} m

1991), after 18 correlation lengths at Borden (Sudicky, 1986), and Welty and Elsner (1997) estimate 10 to 100 correlation lengths may be required in laboratory experiments.

4. Conclusions

Image analysis techniques provide an excellent way to obtain concentration distributions in flow tank experiments where the tracer can be observed through a glass or acrylic wall. The technique is non-intrusive, does not disturb plume dynamics, and provides detailed concentration data over the entire flow domain. One of the key problems with using image analysis techniques in heterogeneous media is the need for separate calibration curves for each type of porous medium due to variations in grain diameter, pore size, and grain color. In addition, with the large dimensions of intermediate-scale experiments it becomes difficult to control lighting uniformity. To address both of these issues a suite of image analysis processing steps were developed and implemented in the widely used MATLAB® environment; the script package can be obtained by contacting the authors. The suite of analysis and visualization tools segments images into optically distinct regions with unique calibration curves and permits the optical determination of tracer concentration in generally heterogeneous media.

As a robust test of our image analysis technique, we applied the processing protocol to an intermediate-scale flow tank (6.25 m long × 1.2 m high × 0.05 m inside width) experiment with a correlated random field of unprecedented heterogeneity and resolution. Twenty-five separate classes of porous media were developed and binned to a synthetic permeability field, creating a field of 3456 rectangular cells (0.096 × 0.020 m), to ensure that the emplaced field closely matched the corresponding statistics of the original continuous distribution.

A tracer pulse of 40 mg/L Rhodamine WT was injected into the heterogeneous field and concentration maps were generated using the image analysis algorithms. The concentration maps are extremely detailed with a spatial resolution of 0.5 × 0.5 mm over the entire area of the 2.5 m long plume. In a further test of the image processing algorithms, imaged concentrations were extracted along the longitudinal axis of the plume and transverse to the plume to allow for the calculation of the experimental coefficients of hydrodynamic dispersion and dispersivities. The closeness of the experimental longitudinal dispersivity to the theoretical asymptotic dispersivity is a verification of the image processing protocol.

The image analysis techniques and the software presented herein provide detailed and accurate concentration distributions for laboratory experiments with minimal equipment and computing needs. The generic approach allows the user complete and easy control of the image processing. While the techniques described above were intended for reflected light images they should be easily adaptable to transmitted light experiments involving non-uniform media properties.

Acknowledgements

This research was funded by the Natural Sciences and Engineering Research Council of Canada through grants awarded to R.A. Schincariol and through scholarships awarded to G.A. Oldenborger.

References

Ababou, R., McLaughlin, D., Gelhar, L.W., Thompson, A.F.B., 1989. Numerical simulation of three-dimensional saturated flow in randomly heterogeneous porous media. Transp. Porous Media 4, 549–565.

Barth, G.R., Illangesekare, T.H., Hill, M.C., Rajaram, H., 2001. A new tracer-density criterion for heterogeneous porous media. Water Resour. Res. 37, 21–31.

Chao, H.C., Rajaram, H., Illangesekare, T.H., 2000. Intermediate-scale experiments and numerical simulations of transport under radial flow in a two-dimensional heterogeneous porous medium. Water Resour. Res. 36, 2869–2884.

Dagan, G., 1982. Stochastic modeling of groundwater flow by unconditional and conditional probabilities. 2. The solute transport. Water Resour. Res. 18, 835–848.

Darnault, C.J.G., DiCarlo, D.A., Bauters, T.W.J., Jacobson, A.R., Throop, J.A., Montemagno, C.D., Parlange, J.Y., Steenhuis, T.S., 2001. Measurement of fluid contents by light transmission in transient-phase oil–water–air systems in sand. Water Resour. Res. 37, 1859–1868.

Detwiler, R.L., Pringle, S.E., Glass, R.J., 1999. Measurement of fracture aperture fields using transmitted light: an evaluation of measurement errors and their influence on simulations of flow and transport through a single fracture. Water Resour. Res. 35, 2605–2617.

Domenico, P.A., Schwartz, F.W., 1998. Physical and Chemical Hydrogeology, 2nd ed. John Wiley and Sons, New York.

Dullien, F.A.L., Dong, M., 1996. Experimental determination of the flow transport coefficients in the coupled equations of two-phase flow in porous media. Transp. Porous Media 25, 97–120.

Garabedian, S.P., LeBlanc, D.R., Gelhar, L.W., Celia, M.A., 1991. Large-scale natural gradient tracer test in sand and gravel, Cape Cod, Massachusetts: 2. Analysis of spatial moments for a non-reactive tracer. Water Resour. Res. 27, 911–924.

Gelhar, L.W., Axness, C.L., 1983. Three-dimensional stochastic analysis of macrodispersion in aquifers. Water Resour. Res. 19, 161–180.

Gheith, H.M., Schwartz, F.W., 1998. Electrical and visual monitoring of small scale three-dimensional experiments. J. Contam. Hydrol. 34, 191–205.

Kasnavia, T., Vu, D., Sabatini, D.A., 1999. Fluorescent dye and media properties affecting sorption and tracer selection. Ground Water 37, 376–381.

Kueper, B.H., Abbott, W., Farquhar, G., 1989. Experimental observations of multiphase flow in heterogeneous porous media. J. Contam. Hydrol. 5, 83–95.

Lee, E.S., Seol, Y., Fang, Y.C., Schwartz, F.W., 2003. Destruction efficiencies and dynamics of reaction fronts associated with the permanganate oxidation of trichloroethylene. Environ. Sci. Technol. 37, 2540–2546.

McNeil, J.D., 2004. Macrodispersion of miscible plumes in correlated heterogeneous permeability fields: advanced processing techniques. M.Sc. Thesis, Department of Earth Sciences, University of Western Ontario, London, Ont. (unpublished).

Oostrom, M., Hayworth, J.S., Dane, J.H., Guven, O., 1992a. Behavior of dense aqueous phase leachate plumes in homogeneous porous media. Water Resour. Res. 28, 2123–2134.

Oostrom, M., Dane, J.H., Guven, O., Hayworth, J.S., 1992b. Experimental investigation of dense solute plumes in an unconfined aquifer model. Water Resour. Res. 28, 2315–2326.

Oostrom, M., Hofstee, C., Lenhard, R.J., Wietsma, T.W., 2003. Flow behavior and residual saturation formation of liquid carbon tetrachloride in unsaturated heterogeneous porous media. J. Contam. Hydrol. 64, 93–112.

Oswald, S., Kinzelbach, W., Greiner, A., Brix, G., 1997. Observation of flow and transport processes in artificial porous media via magnetic resonance imaging in three dimensions. Geoderma 80, 417–429.

Robbins, G.A., 1983. Determining Dispersion Parameters to Predict Groundwater Contamination, Ph.D. thesis, Texas A&M Univ., College Station, Texas, unpublished.

Robin, M.J.L., Gutjhr, A.L., Sudicky, E.A., Wilson, J.L., 1993. Cross-correlated random field generation with the direct Fourier transform method. Water Resour. Res. 29, 2385–2397.

Russ, J.C., 1999. The Image Processing Handbook, 3rd ed. CRC Press, Boca Raton, Florida.

Schincariol, R.A., 1998. Dispersive mixing dynamics of dense miscible plumes: natural perturbation initiation by local-scale heterogeneities. J. Contam. Hydrol. 34, 247–271.

Schincariol, R.A., Schwartz, F.W., 1990. An experimental investigation of variable-density flow and mixing in homogeneous and heterogeneous media. Water Resour. Res. 26, 2317–2329.

Schincariol, R.A., Herderick, E.E., Schwartz, F.W., 1993. On the application of image analysis to determine concentration distributions in laboratory experiments. J. Contam. Hydrol. 12, 197–215.

Schincariol, R.A., Schwartz, F.W., Mendoza, C.A., 1994. On the generation of instabilities in variable density flow. Water Resour. Res. 30, 913–927.

Schwartz, F.W., Zhang, H., 2003. Fundamentals of Ground Water. John Wiley and Sons, New York.

Silliman, S.E., Simpson, E.S., 1987. Laboratory evidence of the scale effects in dispersion of solutes in porous media. Water Resour. Res. 23, 1667–1673.

Silliman, S.E., Zheng, L., Conwell, P., 1998. The use of laboratory experiments for the study of conservative solute transport in heterogeneous porous media. Hydrogeol. J. 6, 166–177.

Simmons, C.T., Pierini, M.L., Hutson, J.L., 2002. Laboratory investigation of variable-density flow and solute transport in unsaturated–saturated porous media. Transp. Porous Media 47, 215–244.

Smart, P.L., Laidlaw, I.M.S., 1997. An evaluation of some fluorescent dyes for water tracing. Water Resour. Res. 13, 15–33.

Sudicky, E.A., 1986. A natural gradient experiment on solute transport in a sand aquifer, spatial variability of hydraulic conductivity and its role in the dispersion process. Water Resour. Res. 22, 2069–2082.

Sutton, D.J., Kabala, Z.J., Fransisco, A., Vasadevan, D., 2001. Limitations and potential of commercially available Rhodamine WT as a groundwater tracer. Water Resour. Res. 37, 1641–1656.

Swartz, C.H., Schwartz, F.W., 1998. An experimental study of mixing and instability development in variable-density systems. J. Contam. Hydrol. 34, 169–189.

Tidwell, V.C., Glass, R.J., 1994. X-ray and visible light transmission for laboratory measurement of two-dimensional saturation fields in thin slab systems. Water Resour. Res. 30, 2873–2882.

Ursino, N., Gimmi, T., Fluhler, H., 2001. Combined effects of heterogeneity, anisotropy, and saturation on steady state flow and transport: a laboratory sand tank experiment. Water Resour. Res. 37, 201–208.

Vasudevan, D., Fimmen, R.L., Francisco, A.B., 2001. Tracer-grade Rhodamine WT: structure of constituent isomers and their sorption behaviour. Environ. Sci. Technol. 35, 4089–4096.

Welty, C., Elsner, M.M., 1997. Constructing correlated random fields in the laboratory for observations of fluid flow and mass transport. J. Hydrol. 202, 192–211.

Wildenschild, D., Jensen, K.H., 1999. Laboratory investigations of effective flow behavior in unsaturated heterogeneous sands. Water Resour. Res. 35, 17–27.

Williamson, S.J., Cumming, H.Z., 1983. Light and color. Nature and Art. John Wiley and Sons, New York, NY.

Wilson, J.F., Cobb, E.D., Kilpatrick, F.A., 1986. Fluorometric procedures for dye tracing. Techniques of Water Resources Investigations of the United States Geological Survey: Book 3, Applications of Hydraulics, USGS.